Supplementary Information

Structure, stability and electronic properties of two-dimensional monolayer noble metals with triangular lattices: Cu, Ag, and Au

Zhefeng Wang,[a] Kai Chen,[a] Youmin Xu,[a] Zengjie Wang,[a] Lingbao Kong,[a] Songyou Wang,*[abc] and Wan-Sheng Su,*[def]

Author affiliations:
* Corresponding authors
[a]Shanghai Ultra-Precision Optical Manufacturing Engineering Center, Department of Optical Science and Engineering, Fudan University, Shanghai 200433, China
E-mail: songyouwang@fudan.edu.cn
Tel: +86 216 564-2970
[b]Yiwu Research Institute of Fudan University, Chengbei Road, Yiwu City, 322000 Zhejiang, China
[c]State Key Laboratory of Photovoltaic Science & Technology Laboratory, Institute of Optoelectronics, Fudan University, Shanghai 200433, China
[d]National Taiwan Science Education Center, Taipei 111081, Taiwan
E-mail: wssu@mail.ntsec.gov.tw
Tel: +886-2-6610-1234
[e]Department of Electro-Optical Engineering, National Taipei University of Technology, Taipei 106344, Taiwan
[f]Department of Physics, National Sun Yat-sen University, Kaohsiung 804201, Taiwan

Table of Contents:

Section S1: Geometry Optimization of Primitive Cells in Different Sizes

Section S2: AIMD Simulations at Elevated Temperatures

Section S3: Convergence Tests

Section S4: GGA+PBE Calculations

Section S5: Band Structures of Bulk and Monolayer Noble Metals

Section S6: Phonon Spectra Calculations with Different Pseudopotentials

References

Section S1: Geometry Optimization of Primitive Cells in Different Sizes

Five types of primitive cells were used in the calculations, as shown in Fig. S1. For ease of reference, these primitive cells are labeled N, F, Y, X, and U, respectively, and are marked in Fig. S1. The primitive cell used in our manuscript is labeled U. All parameters are consistent with those in the text, and the K-point grid is scaled accordingly to maintain the same sampling spacing.

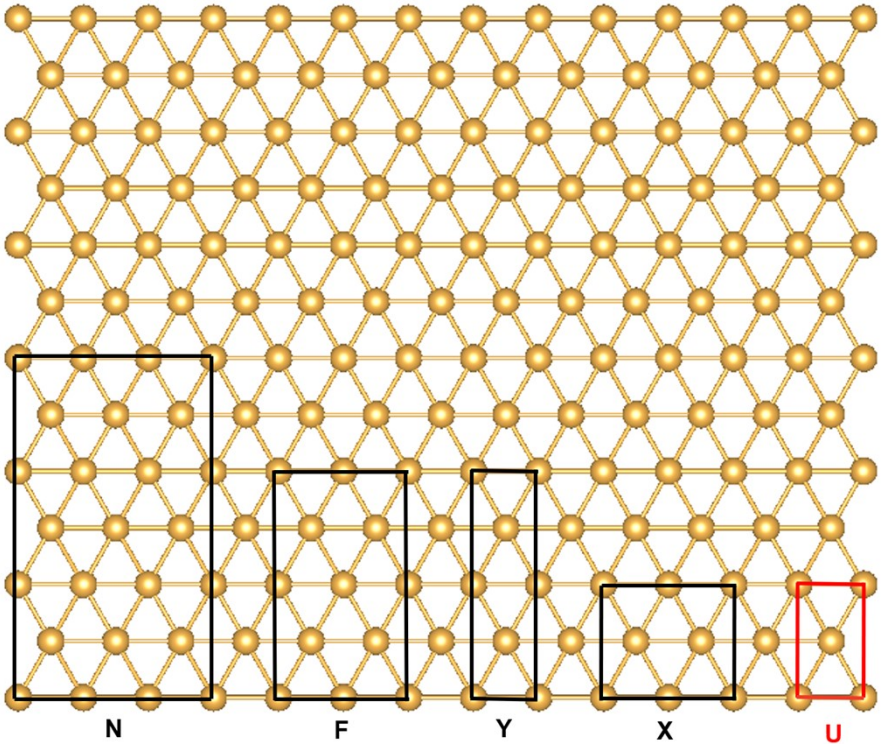

Figure S1. Diagram of infinite 2D metal monolayers with various primitive cells marked by lines. 'U' denotes the primitive cell used in this study.

Table S1. Average bond length of different primitive cells after optimization.

Bond length (Å)	Au	Ag	Cu
N	2.687	2.700	2.359
F	2.687	2.700	2.359
Y	2.687	2.700	2.359
X	2.686	2.701	2.360
U (Paper used)	2.687	2.700	2.359

Average	2.687±0.001	2.700±0.001	2.700±0.001

As listed in Table S1, the bond lengths of the different primitive cells are nearly identical. In the four primitive cells tested, all triangles are standard isosceles, with bond length variations of less than 0.1%. Therefore, no significant size-induced drifts are observed in these 2D monolayers.

Section S2: AIMD Simulations at Elevated Temperatures

The results are shown in Figs. S2 and S3. As seen in Fig. S3, Au exhibits the highest thermal stability among the three materials, followed by Cu, while Ag is the most susceptible to thermal degradation, particularly at elevated temperatures. At low temperatures (300 K and 500 K), all three materials exhibit good stability, maintaining intact structures with no significant thermal ripples. At intermediate temperatures (1000 K and 1200 K), Ag shows significantly reduced stability compared to Cu and Au. Notably, at 1200 K, voids begin to form in the Ag structure due to its weaker bonding, while Cu shows increased thermal motion, and Au remains relatively stable. At high temperatures (1400 K and 1500 K), structural breakdown becomes evident for all three metals, with Ag being the least stable, experiencing significant void formation and lattice collapse. In contrast, Cu and Au exhibit better resistance to thermal disruption, with Au showing the highest overall thermal stability. These findings suggest that Au is the most suitable candidate for high-temperature applications, such as nanoelectronics, while Ag may require additional stabilization measures for practical use.

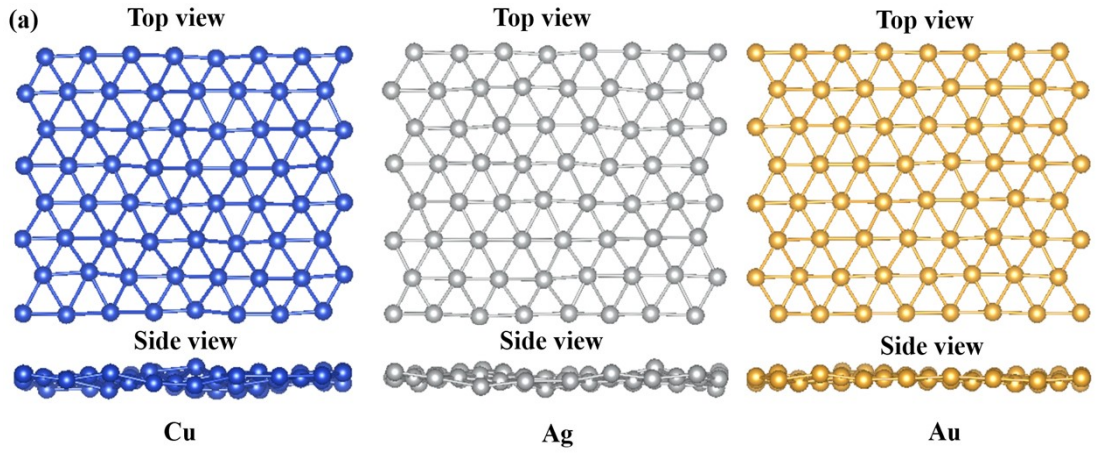

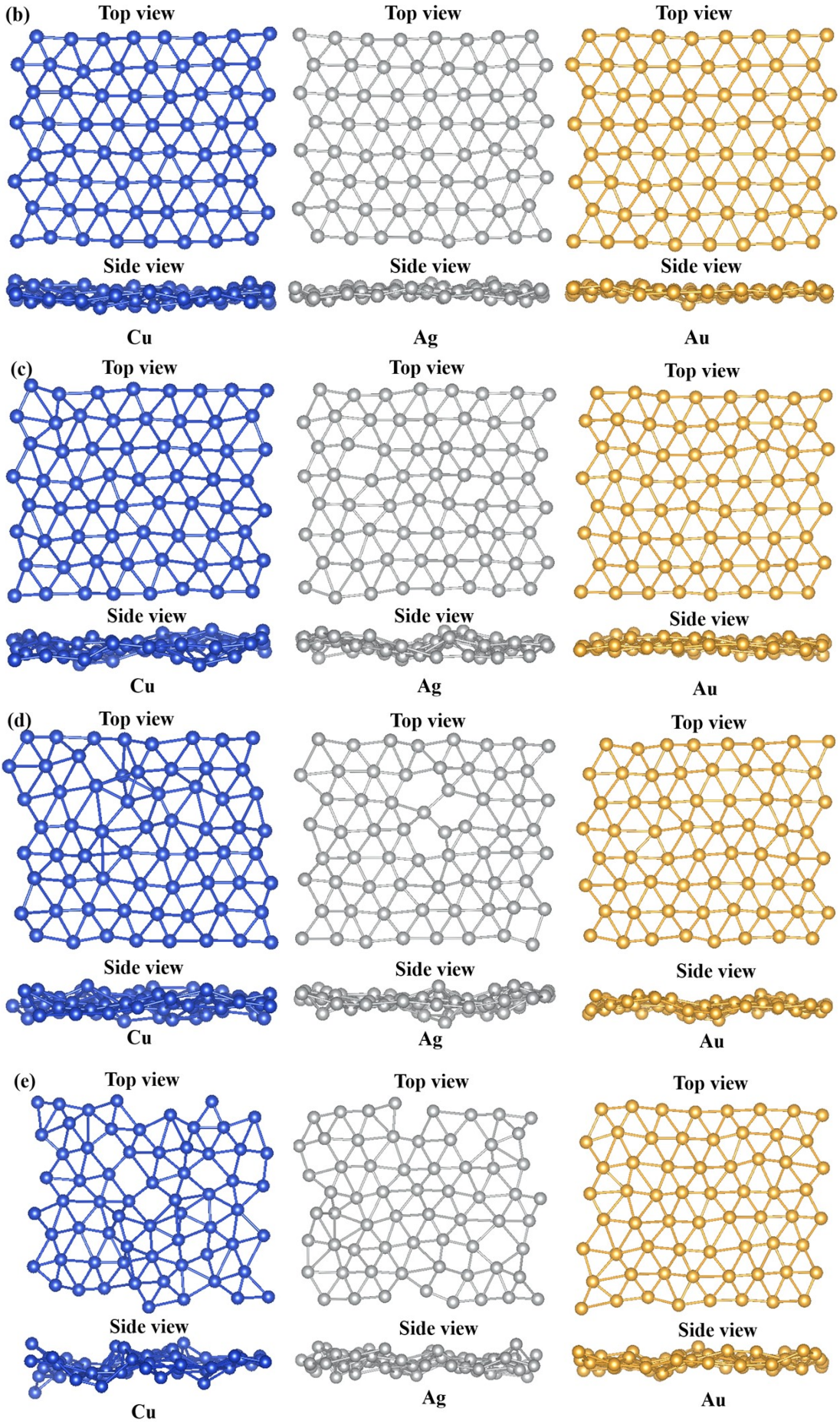
(b)
Top view
Top view
Top view
Side view
Side view
Side view
Cu
Ag
Au
(c)
Top view
Top view
Top view
Side view
Side view
Side view
Cu
Ag
Au
(d)
Top view
Top view
Top view
Side view
Side view
Side view
Cu
Ag
Au
(e)
Top view
Top view
Top view
Side view
Side view
Side view
Cu
Ag
Au

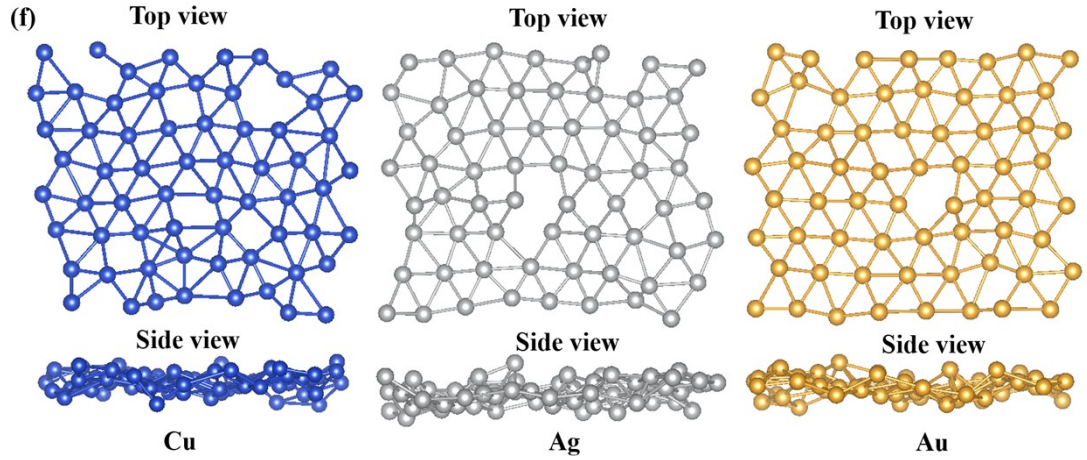

Figure S2. Top and side views of the final frames after a 10 ps AIMD simulation at (a) 300 K, (b) 500 K, (c) 1000 K, (d) 1200 K, (e) 1400 K, and (f) 1500 K.

The structural changes of the Cu, Ag, and Au 2D monolayers are also reflected in the variation of their potential energy over time at different temperatures, as shown in Fig. S3. At 300 K and 500 K, the potential energy remains stable, indicating minimal structural disruption. However, at 1000 K and 1200 K, the potential energy (PE) begins to exhibit an upward trend (PE increasing) for all three materials, corresponding to the emergence of thermally induced ripples and voids in Ag, as well as local distortions in Cu. At 1400 K and 1500 K, the potential energy increases significantly, aligning with the severe structural degradation observed in Ag and Cu, while Au maintains relatively better stability. These trends underscore the direct relationship between temperature-induced structural changes and the stability of 2D metal monolayers.

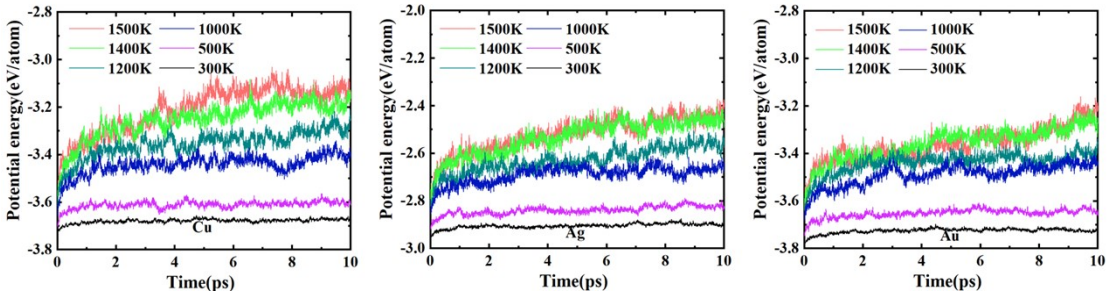

Figure S3. The potential energy of the three 2D noble metal monolayers during AIMD simulations at varying temperatures.

Section S3: Convergence Tests

A series of convergence tests were performed to verify the accuracy of the calculations and ensure the appropriateness of the *K*-point grid as well as the energy/force convergence criteria. In each set of tests, parameters were consistent with those described in the 'Computational Details' section of the manuscript, except for the variables being tested.

A $M \times N \times 1$ Monkhorst-Pack[1] *K*-point mesh was used in calculations, where N was varied, and M adjusted accordingly to maintain a roughly uniform sampling density in both directions of the Brillouin zone. As shown in Fig. S4, after the initial oscillation, the system's energy gradually converges. Therefore, the $22 \times 12 \times 1$ *K*-point mesh we used provides sufficient accuracy.

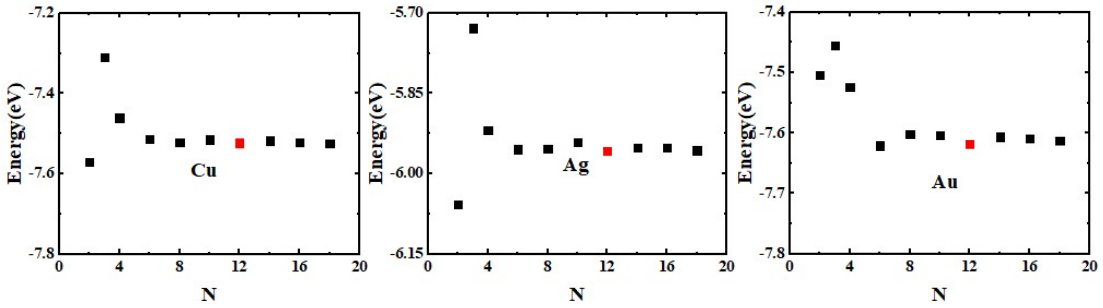

Figure S4. Energy of the three 2D noble metal monolayers calculated using different K-point meshes. M varies with N to maintain consistent sampling spacing in both directions of the Brillouin zone.

The tests for energy and force convergence criteria were carried out simultaneously. The specific values of each set of parameters are listed below. Results are shown in Figure S5. The energy values calculated using different parameters are nearly identical, indicating that the convergence criteria employed ensure sufficient accuracy.

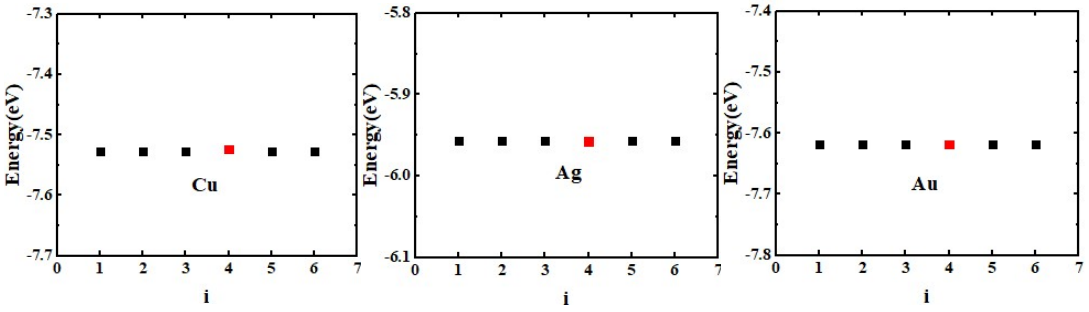

Figure S5. Energy of the three 2D noble metal monolayers calculated using various convergence criteria.

Table S2. Calculation parameters for EDIFF and EDIFFG.

Number (i)	EDIFF (eV per atom)	EDIFFG (eV Å^{-1})
1	10^{-5}	10^{-2}
2	10^{-6}	5×10^{-3}
3	10^{-7}	10^{-3}
4	10^{-8}	10^{-3}
5	10^{-9}	5×10^{-4}
6	10^{-10}	10^{-4}

Section S4: GGA+PBE Calculations

The exchange–correlation energy functional of electrons is described using the projector augmented wave (PAW)[2] method with the Perdew–Burke–Ernzerh (PBE)[3] functional within the generalized gradient approximation (GGA). All other settings align with those outlined in the 'Computational Details' section.

Table S3. Lattice constants of three 2D noble metal monolayers after optimization using GGA+PBE.

Lattice constants (Å)	Au	Ag	Cu
a	2.743	2.793	2.437
b	4.756	4.847	4.226

Table S4. Bond angles of three 2D noble metal monolayers after optimization.

Bond angle (deg)	Au	Ag	Cu
α	60.12	60.20	60.11
β	59.77	59.62	59.78

Tables S3 and S4 list the optimized lattice constants of Cu, Ag, and Au. The average bond length of goldene is 2.740 Å, which is not as close to the experimental value of 2.62 Å as the result obtained using the LDA+USPP method. Additionally, when considering the bond angles, these lattices exhibit lower symmetries.

The band structures of the three 2D noble metal monolayers, calculated using GGA+PBE and LDA+USPP, are shown in Fig. S6. A comparison of the results reveals that the band structures obtained by both methods are similar, displaying metallic behavior.

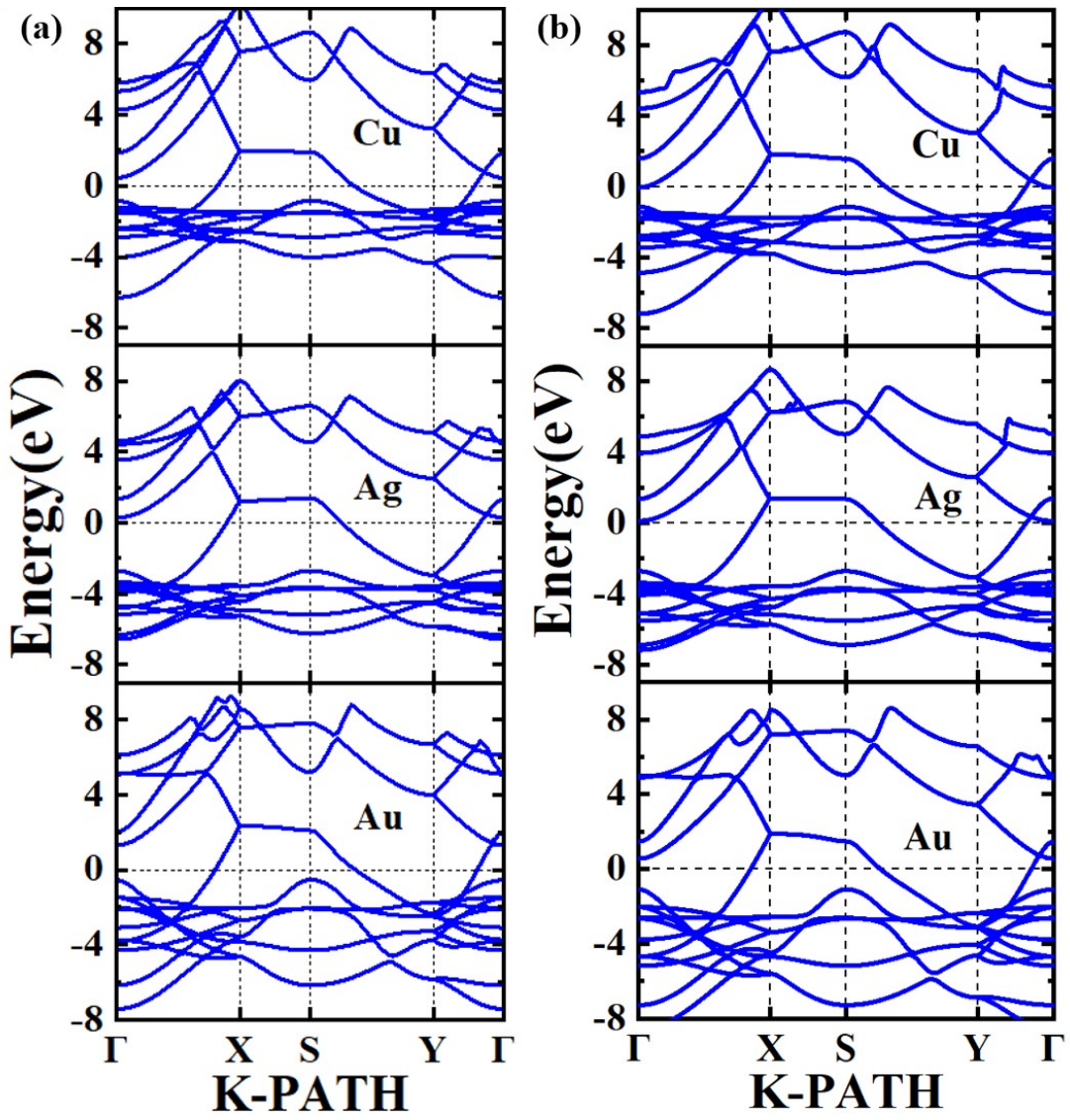

Figure S6. The calculated band structures of three 2D noble metals are presented using: (a) GGA+PBE method and (b) LDA+USSP method.

Section S5: Band Structures of Bulk and Monolayer Noble Metals

Figures S7(a) and S7(b) present the calculated band structures of Cu, Ag, and Au in both the face-centered cubic (FCC) lattice and monolayer configurations, respectively. FCC primitive cells containing one atom are used. All settings align with those outlined in the 'Computational Details' section, except for the *K*-path. The electronic properties of both the 2D monolayers and 3D bulk materials exhibit metallic behavior.

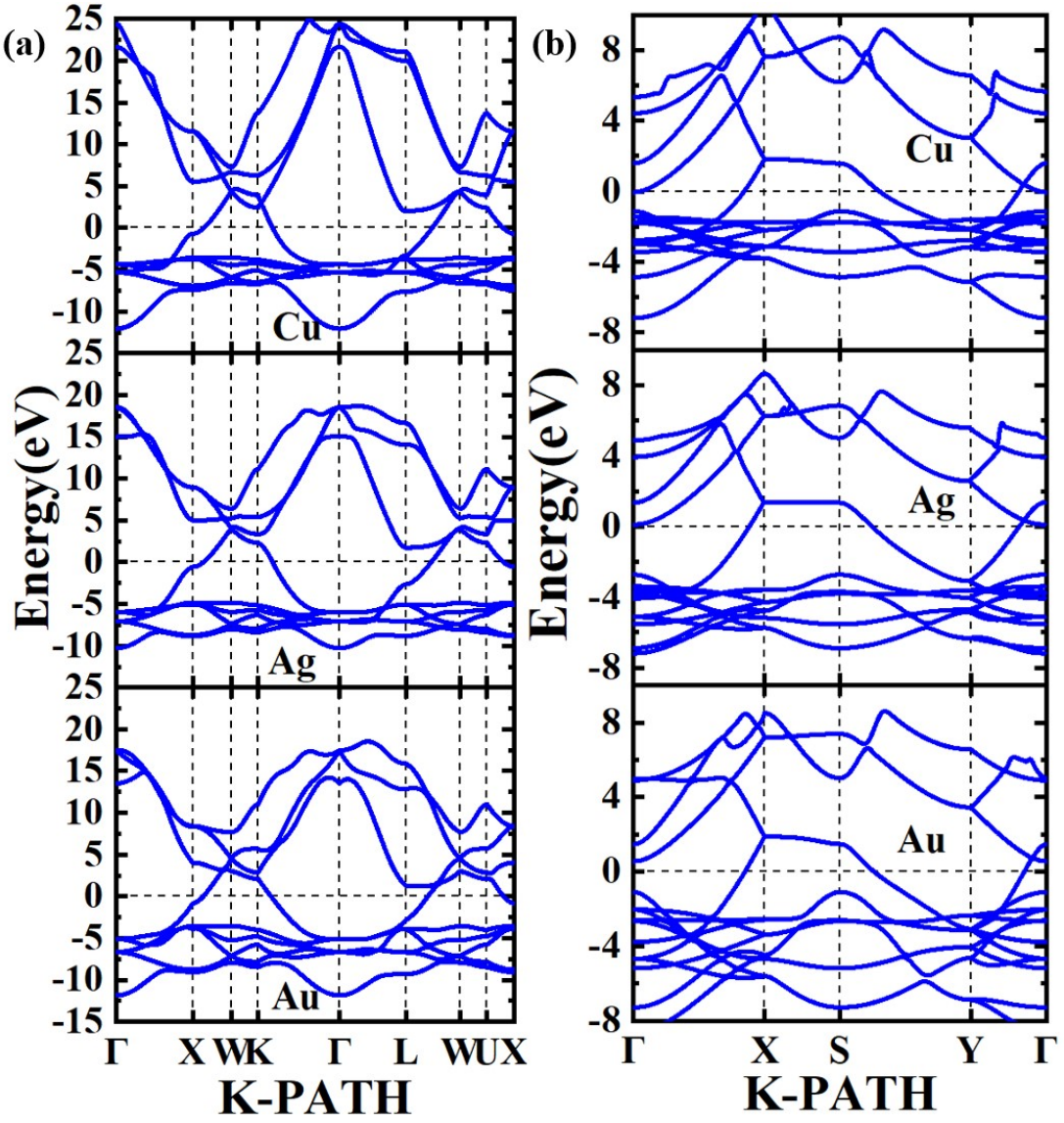

Figure S7. Energy band structures of 3D bulk FCC and 2D monolayers of Cu, Ag and Au: (a) Band structures of 3D FCC Cu, Ag and Au, (b) Band structures of 2D monolayers of Cu, Ag and Au.

Section S6: Phonon Spectra Calculations with Different Pseudopotentials

Different pseudopotentials and software were employed to analyze kinetic stability. Phonon spectra calculations were performed within the LDA framework using VASP and ultrasoft pseudopotentials. The results from the other two methods are presented in Figure S8, where PAW-PBE[2, 3] pseudopotentials in VASP[4, 5] and norm-conserving[6] pseudopotentials in CASTEP[7] were used to generate the data shown in panels (a) and (b) of Figure S8. Notably, the phonon spectra of Cu, calculated with PAW-PBE pseudopotentials, exhibit negative frequencies.

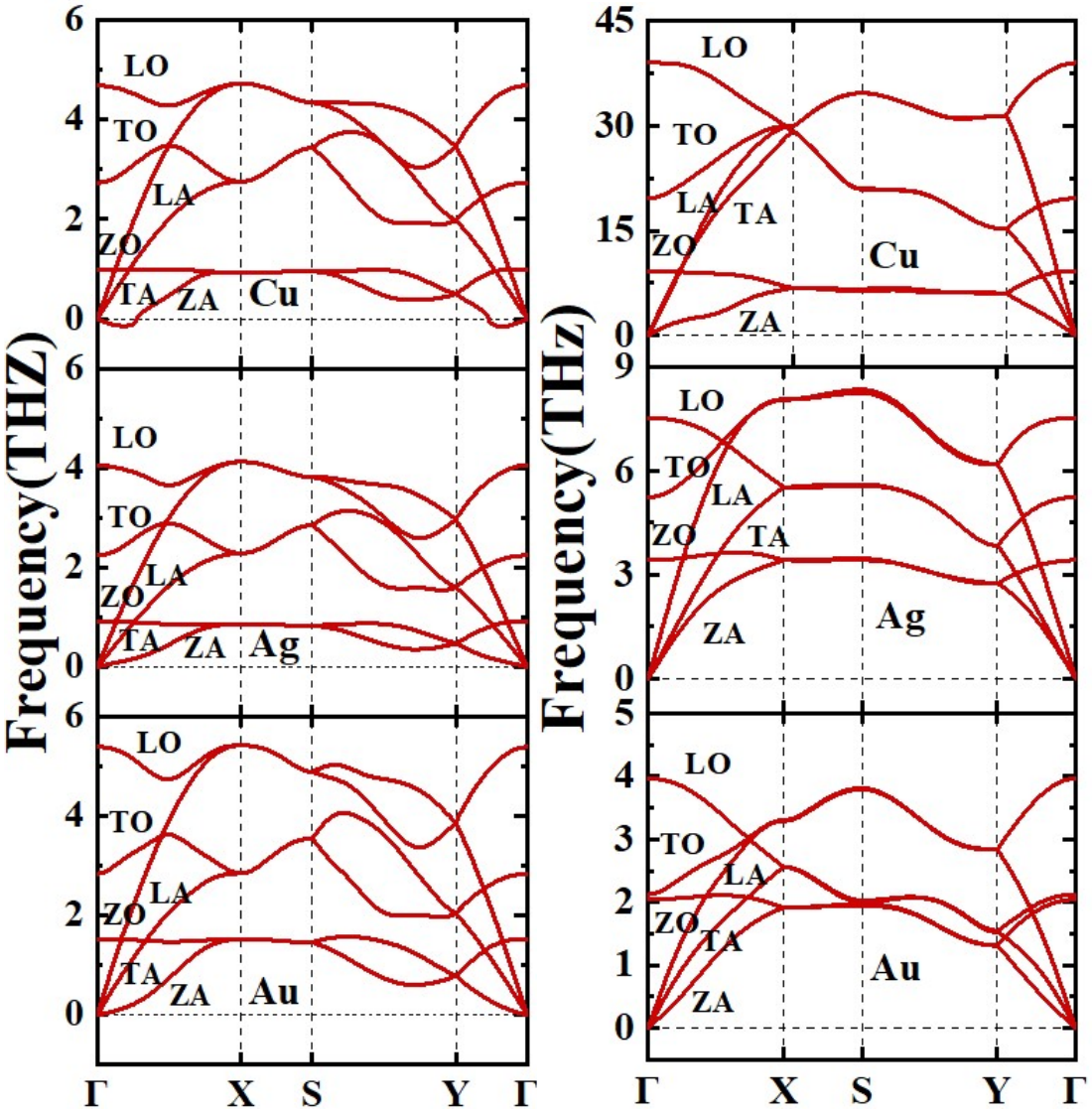

Figure S8. Phonon spectra of the three 2D noble metal monolayers calculated using different methods: (a) PAW-PBE pseudopotentials in VASP, and (b) norm-conserving pseudopotentials in CASTEP.

References:

1. H. J. Monkhorst and J. D. Pack, *Physical Review B*, 1976, **13**, 5188-5192.
2. G. Kresse and D. Joubert, *Physical Review B*, 1999, **59**, 1758-1775.
3. J. P. Perdew, K. Burke and M. Ernzerhof, *Physical Review Letters*, 1996, **77**, 3865-3868.
4. G. Kresse and J. Furthmüller, *Computational Materials Science*, 1996, **6**, 15-50.
5. G. Kresse and J. Hafner, *Physical Review B*, 1994, **49**, 14251-14269.
6. D. R. Hamann, M. Schlüter and C. Chiang, *Physical Review Letters*, 1979, **43**, 1494-1497.
7. S. J. Clark, M. D. Segall, C. J. Pickard, P. J. Hasnip, M. I. J. Probert, K. Refson and M. C. Payne, *Zeitschrift für Kristallographie - Crystalline Materials*, 2005, **220**, 567-570.